Supplementary materials for "Multifunctional Acoustic and Mechanical Metamaterials Prepared from Continuous CFRP Composites"

Zhen-Yu Li [a#]**, Hong-Ze Li** [b#]**, Jin-Shui Yang** [b, c*]**, Li Ma** [d]**, Xin-Tao Wang** [b]**, Yuan-Yuan Gao** [a]**,**

Bin-Gang Xu [a]**, Jian Xiong** [d]**, Hong Hu** [a**]

[a] *School of Fashion and Textiles, The Hong Kong Polytechnic University, Hung Hom, Kowloon,*
Hong Kong, China

[b] *College of Aerospace and Civil Engineering, Harbin Engineering University,*
Harbin 150001, PR China

[c] *Qingdao Innovation and Development Base, Harbin Engineering University,*
Qingdao 266000, PR China

[d] *Center for Composite Materials, Harbin Institute of Technology, Harbin 150001, China*

———————————————

[#] Both authors contributed equally to this article

[*] Corresponding author,

E-mail addresses: yangjinshui@hrbeu.edu.cn (J.-S. Yang).

[**] Corresponding author,

E-mail addresses: hu.hong@polyu.edu.hk (H. Hu).
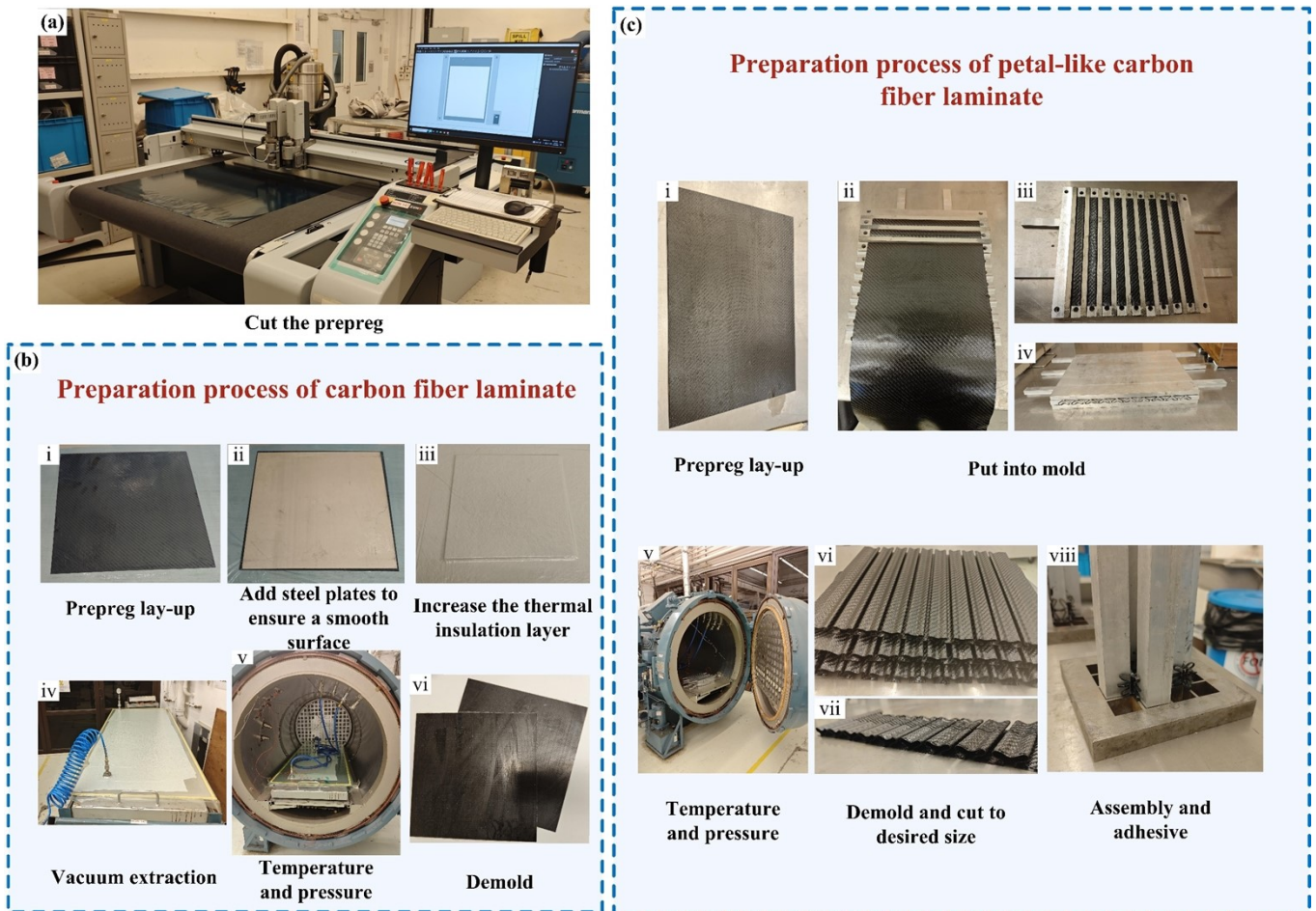
Part 1: Key manufacturing steps

Fig. S1 Key manufacturing steps for multifunctional composite structures. (a) Prepreg cutting. (b) Preparation steps of carbon fiber laminates. (c) Preparation steps of carbon fiber petal-like corrugated plates.

Part 2: Some dimensional parameters and mechanical properties of the material

In pursuit of achieving a composite petal-like structure with superior mechanical properties alongside exceptional acoustic characteristics, our methodology entailed the precise cutting of carbon fiber plates and membranes into various shapes. By strategically assembling these components, unique internal cavities were formed. In the case of 2D petal-like structures, each cell corresponded to a small cavity with perforation strategically located at the center of each cell to facilitate optimal sound wave propagation. Detailed parameters for components P_2-P_5 and M_2 can be found in **Fig. S2**. In the context of 3D petal-like structures, meticulous consideration was given to compression direction and assembly procedures when selecting perforation locations. Components P_1, M_1, P_3, and M_3, vital for the assembly of the 3D structure, were individually cut and prepared. To ensure seamless fit within the impedance tube, the TPU material frames with varying volume fractions were created using selective laser sintering (SLS) technology. The material properties of the PEI membranes

include a density of 1270 kg/m³, modulus of 3.3 GPa, and a Poisson ratio of 0.36. Similarly, the TPU material is characterized by a density of 1177 kg/m³, modulus of 35.40 MPa, and a Poisson ratio of 0.4.
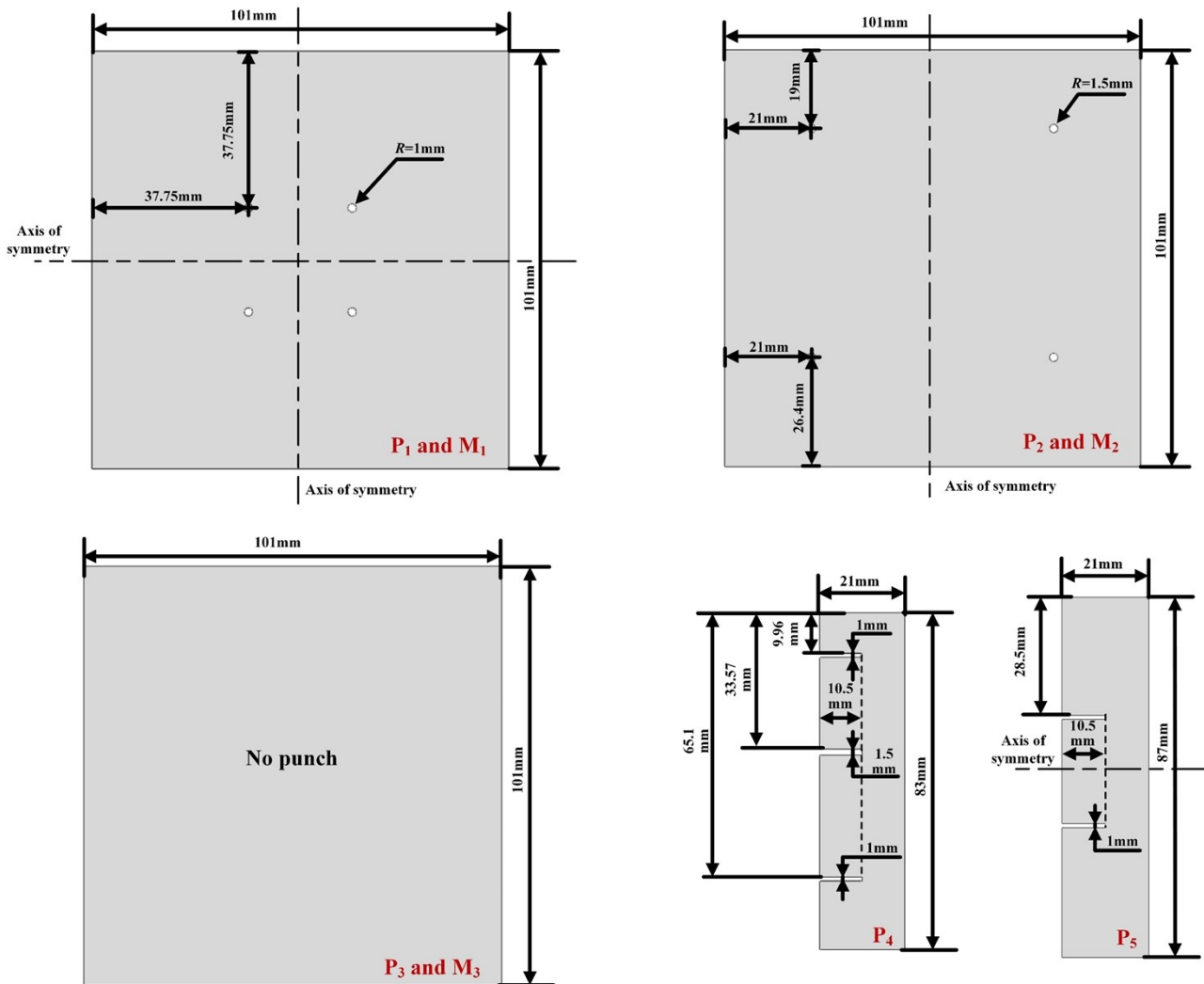

Fig. S2 Cutting parameters of carbon fiber sheets and membranes.

Part 3: Finite element analysis method of mechanical properties

Using ABAQUS/Explicit software, this study simulated the fiber-reinforced petal-like structures under quasi-static uniaxial compression. The platen was represented as discrete rigid, and the structure was meshed using eight-node 3D reduced-integral solid elements (C3D8R) after performing convergence analysis with a mesh size of 0.5mm. The petal-like strips were combined to establish hard contact and tangential frictionless behavior in line with the experiment. The lower platen was completely fixed, replicating the experimental setup, while the upper platen was constrained in all directions except vertically. To model the deformation and failure of composite structures, a vector

user material subroutine (VUMAT) was implemented.

The modified 3D Hashin's failure criterion and Yeh delaminational failure criteria are used into damage initiation model. In composite laminates, five damage modes can be summarized: fiber tensile fracture, fiber compression fracture, matrix tensile fracture, matrix compression fracture and delamination failure. The corresponding five types of failure modes are defined as:

(a) Fiber stretching ($\varepsilon_{11} > 0$):

$$R_{ft}^2 = \left(\frac{\varepsilon_{11}}{X_T^\varepsilon}\right)^2 + \left(\frac{\varepsilon_{12}}{S_{12}^\varepsilon}\right)^2 + \left(\frac{\varepsilon_{13}}{S_{13}^\varepsilon}\right)^2$$

(1)

(b) Fiber compression ($\varepsilon_{11} \leq 0$):

$$R_{fc}^2 = \left(\frac{\varepsilon_{11}}{X_C^\varepsilon}\right)^2$$

(2)

(c) Matrix tension ($\varepsilon_{22} + \varepsilon_{33} \geq 0$):

$$R_{mt}^2 = \left(\frac{\varepsilon_{11} + \varepsilon_{33}}{Y_T^\varepsilon}\right)^2 + \left(\frac{1}{S_{23}^\varepsilon}\right)^2\left(\varepsilon_{23}^2 - \frac{E_{22}E_{23}}{G_{23}^2}\varepsilon_{22}\varepsilon_{33}\right)^2 + \left(\frac{\varepsilon_{12}}{S_{12}^\varepsilon}\right)^2 + \left(\frac{\varepsilon_{13}}{S_{13}^\varepsilon}\right)^2$$

(3)

(d) Matrix compression ($\varepsilon_{22} + \varepsilon_{33} < 0$):

$$R_{mc}^2 = \left(\frac{E_{22}\varepsilon_{22} + E_{33}\varepsilon_{33}}{G_{12}S_{12}^\varepsilon}\right)^2 + \left(\frac{\varepsilon_{22} + \varepsilon_{33}}{Y_C^{\varepsilon 2}}\right)\left[\left(\frac{E_{22}Y_C^\varepsilon}{2G_{12}S_{12}^\varepsilon}\right)^2 - 1\right] + \left(\frac{1}{S_{23}^\varepsilon}\right)^2\left(\varepsilon_{23}^2 - \frac{E_{22}E_{23}}{G_{23}^2}\varepsilon_{22}\varepsilon_{33}\right)^2 + \left(\frac{\varepsilon_{12}}{S_{12}^\varepsilon}\right)^2 + \left(\frac{\varepsilon_{13}}{S_{13}^\varepsilon}\right)^2$$

(4)

(e) Delamination failure ($\varepsilon_{33} \geq 0$):

$$R_{ld}^2 = \left(\frac{\varepsilon_{33}}{Z_T^\varepsilon}\right)^2 + \left(\frac{\varepsilon_{13}}{S_{13}^\varepsilon}\right)^2 + \left(\frac{\varepsilon_{23}}{S_{23}^\varepsilon}\right)^2$$

(5)

where $X_T^\varepsilon, X_C^\varepsilon$ are longitudinal tensile and compressive ultimate strain of composite laminates respectively, $Y_T^\varepsilon, Y_C^\varepsilon$ are transverse tensile and compressive ultimate strain respectively, $S_{23}^\varepsilon, S_{12}^\varepsilon$ and S_{13}^ε are in-plane and out-plane shear ultimate strain respectively, Z_T^ε is tensile delamination ultimate strain. Failure factor $R_i (i = ft, fc, mt, mc, ld)$ represents the failure level. These limit strain components are defined as follows:

$$X_T^\varepsilon = \frac{X_T}{E_{11}}, \quad X_C^\varepsilon = \frac{X_C}{E_{11}}, \quad Y_T^\varepsilon = \frac{Y_T}{E_{11}}, \quad Y_C^\varepsilon = \frac{Y_C}{E_{22}}, \quad Z_T^\varepsilon = \frac{Z_T}{E_{33}}, \quad S_{12}^\varepsilon = \frac{S_{12}}{G_{12}}, \quad S_{13}^\varepsilon = \frac{S_{13}}{G_{13}}, \quad S_{23}^\varepsilon = \frac{S_{23}}{G_{23}}$$

(6)

The damage variable d_i is introduced into the damage evolution process to characterize the damage degree of composites. The definition domain of damage variable d_i is [0,1]. If $d_i = 0$, there is no damage; when $d_i = 1$, the composite material completely lost its mechanical properties. When

damage occurs ($d_i > 0$), the corresponding mechanical properties (elastic modulus) begin to deteriorate. The relationship d_i with R_i is shown in Equation (7):

$$d_i = \begin{cases} 0 & (R_i < 1) \\ 1 - \dfrac{1}{R_i^m} & (R_i \geq 1) \end{cases}, (i = ft, fc, mt, mc, ld) \quad (7)$$

where m ($m > 0$) is the non-dimensional parameter to control the stiffness degradation rate of composite material. At time t, the damage variable as:

$$d_i^t = \max\left(d_i^\tau, 0\right), (\tau \leq t; i = ft, fc, mt, mc, ld) \tag{8}$$

Based on damage variation, the stress-strain relationship of laminates can be expressed as:

$$\begin{Bmatrix} \varepsilon_{11} \\ \varepsilon_{22} \\ \varepsilon_{33} \\ \gamma_{12} \\ \gamma_{23} \\ \gamma_{13} \end{Bmatrix} = \begin{bmatrix} \dfrac{1}{E_{11}(1-\omega_1)} & -\dfrac{v_{12}}{E_{22}} & -\dfrac{v_{13}}{E_{33}} & & & \\ -\dfrac{v_{12}}{E_{22}} & \dfrac{1}{E_{22}(1-\omega_2)} & -\dfrac{v_{23}}{E_{22}} & & 0 & \\ -\dfrac{v_{13}}{E_{33}} & -\dfrac{v_{23}}{E_{22}} & \dfrac{1}{E_{33}(1-\omega_3)} & & & \\ & & & \dfrac{1}{G_{12}(1-\omega_4)} & 0 & 0 \\ & 0 & & 0 & \dfrac{1}{G_{23}(1-\omega_5)} & 0 \\ & & & 0 & 0 & \dfrac{1}{G_{13}(1-\omega_6)} \end{bmatrix} \begin{Bmatrix} \sigma_{11} \\ \sigma_{22} \\ \sigma_{33} \\ \tau_{12} \\ \tau_{23} \\ \tau_{13} \end{Bmatrix} \tag{9}$$

where damage parameter $\omega_i = (i = 1, \cdots, 6)$ is defined as:

$$\omega_1 = \max(0, d_f), \omega_2 = \max(0, d_f, d_m), \omega_3 = \max(0, d_f, d_d), \omega_4 = \max(0, d_f, d_m), \omega_5 = \max(0, d_f, d_d), \omega_6 = \max(0, d_f, d_d),$$

$$d_f = \max(0, d_{ft}, d_{fc}), d_m = \max(0, d_{mt}, d_{mc}), d_d = \max(0, d_{ld}) \tag{10}$$

According to the failure criterion, the unit stiffness will degenerate when a unit fails. Therefore, the maximum strain criterion is applied in the VUMAT subroutine to remove the distorted elements. Furthermore, considering the debonding damage was not the mainly damage models for the present composite Petal-like structures, and the simulation of debonding generally requires vast computing capacity and time, the simulation of the debonding between strips was ignored.

Given the inherent uncertainty surrounding structural failure and the demanding computational performance needed for extensive iterative calculations, finite element analysis emerges as the predominant technique employed to model the initiation of loading and failure mechanisms within structures. Notably, **Fig. S3** delineates the moduli, Poisson's ratios, stress-strain profiles, and failure modalities for two distinct structures subjected to quasi-static compressive loading conditions. Evidently, the outcomes elucidate the capability of the finite element method in effectively capturing both the linear and nonlinear phases of structural behavior.
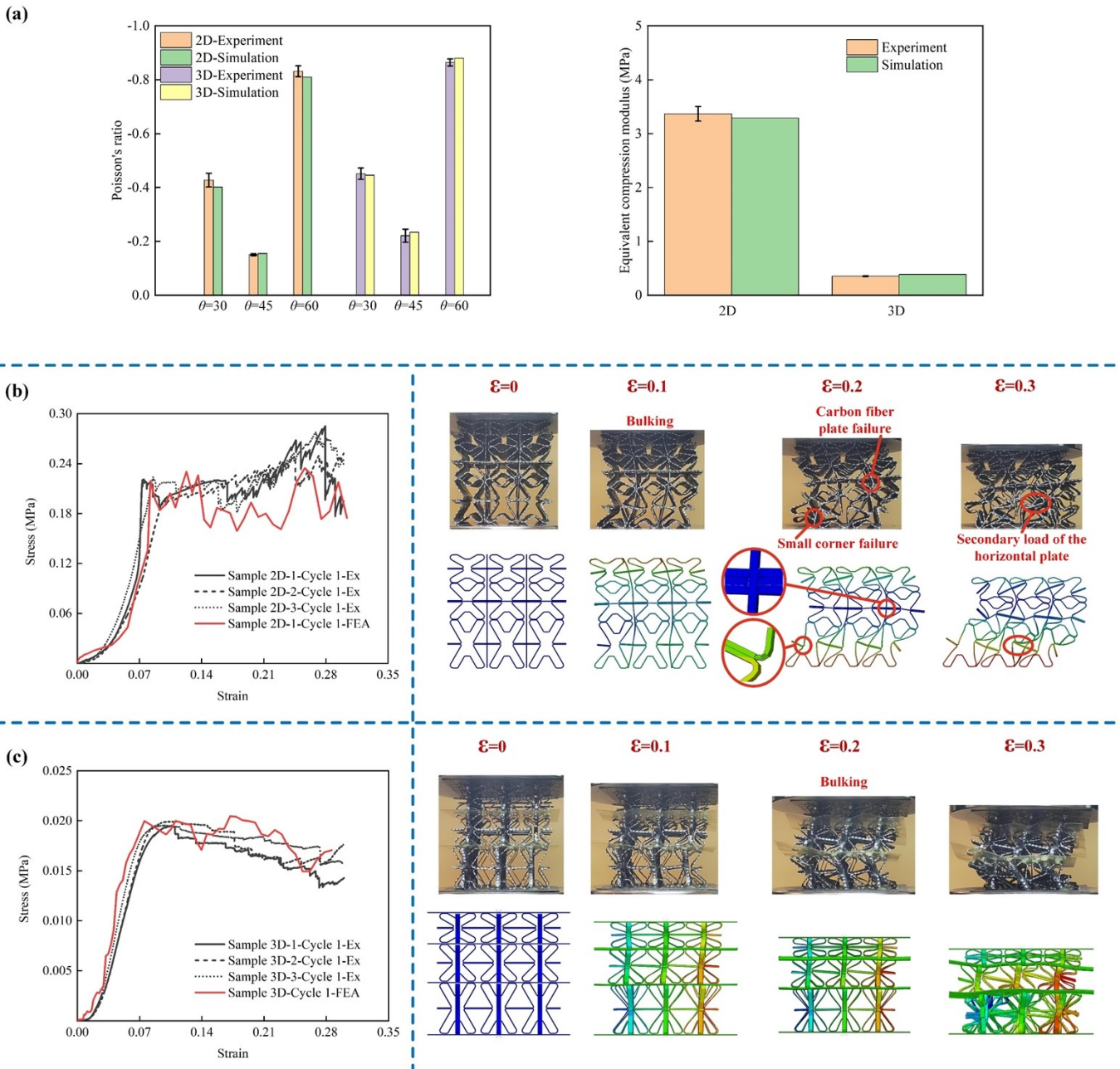
Fig. S3 Comparison between finite element and experiment of structures under compression load. (a) Poisson's ratio and equivalent compression modulus. (b) Comparison of stress-strain curves and failure modes of 2D structures under compressive loads. (c) Comparison of stress-strain curves and failure modes of 3D structures under compressive loads.

Part 4: Theoretical derivation for sound insulation and absorption

The assessment of noise reduction performance in structures is conducted by utilizing SAC and STL as key evaluation parameters. Initially, the sound channel extending in all directions of the 2D petal-like structure is conceptualized as an elongated narrow cavity. It is imperative to emphasize the maintenance of the area of the upper surface of the cavity during the execution of the cavity equivalent

process. Simultaneously, the hole depth of the single-layer Helmholtz cavity is maintained at the cumulative sum of the hole depths of the 3-layer perforated structure within the 2D petal-like structure, while ensuring a constant aperture. Our parametric analysis has revealed that labyrinth structures of identical apertures and cavity volumes exhibit sound absorption peaks at consistent frequencies. Accordingly, the focus of our investigation pertains to the examination of the resonance properties of Chamber I and Chamber IV, as portrayed in **Fig. 1(a) (iii)**. The resonant cavity equivalent model is shown in **Fig. S4(a)**, and the SAC can be obtained by the impedance matching method. The real and imaginary parts of the impedance are as follows[1]:

$$
\begin{cases}
r_{s,i} = \dfrac{8\delta l}{s_i \rho_0 c_0 a_i^2}\left[(1+\dfrac{\beta_i^2}{32})^{\frac{1}{2}} + \dfrac{\sqrt{2}\beta_i a_i}{4l}\right] \\
x_{s,i} = \dfrac{kl}{s_i}\left[1 + (9+\dfrac{\beta_i^2}{2})^{-\frac{1}{2}} + 1.7\dfrac{a_i}{l}\right] - \cot(kd')
\end{cases}
,\#(11)
$$

where $r_{s,i}$ and $x_{s,i}$ represent the real and imaginary parts of the normalized surface impedance of each resonator unit cell. a_i denotes the radius of each hole in the perforated plate, s_i denotes the surface porosity of the unit cell, and l is the neck length. Simultaneous, δ denotes the kinematic viscosity of air, β_i is the perforation constant for each unit cell, which can be expressed as: $\beta_i = a_i\sqrt{\rho_0\omega/\delta}$. Based on the air condition, the impedance of air can be expressed as $Z_0 = \rho_0 c_0$, and the wave velocity can be expressed as $k = 2\pi f/c_0$. Achieving equalization of the cavity height demonstrates a single-layer equivalent cavity height of d'. Utilizing the aforementioned methodology, we are able to calculate the normalized surface impedance Z_s of the two resonant cavities as a means of determining the structural reflection coefficient r. The formula is shown below:

$$
r = \frac{Z_s - 1}{Z_s + 1} = \frac{\sum\limits_{i=1}^{2} Z_{s,i} - 1}{\sum\limits_{i=1}^{2} Z_{s,i} + 1} = \frac{\sum\limits_{i=1}^{2} r_{s,i} + jx_{s,i} - 1}{\sum\limits_{i=1}^{2} r_{s,i} + jx_{s,i} + 1}.\#(12)
$$

The SAC of the structure can be calculated from the reflection coefficient expressed as follows:

$$
SAC = 1 - |r|^2.\#(13)
$$

The low-frequency SACs (below 500 Hz) obtained by theoretical derivation and numerical simulation of the structure are shown in **Fig. S4(a)**. The accuracy of the simulation method can be verified by the comparison of the results.

On the other hand, upon examination of the sound insulation capabilities of the 3D petal-like

structure, it is posited that the individual layers of the petal-like core contribute to enhancing the structural load-bearing capacity and offer a potential alternative to supplementary MAM additional blocks for achieving localized resonance. Simultaneously, numerous points of contact exist between the petal-like core layer and the membrane, resulting in the formation of interrelationships that contribute to the amplification of low-frequency anti-resonance of the MAM. This mechanism enhances the sound insulation properties of the metamaterial across a wide range of low frequencies. To facilitate calculations, a single-layer MAM with a petal-shaped core layer is selected as the focal point of investigation to elucidate the impact of core layers on sound insulation performance. The single-layer MAM carrying a petal-like core layer and its equivalent model are shown in **Fig. S4(b)**.

In this study, we investigate the application of inertia force at the contact position of a petal-like core layer with a membrane to achieve equilibrium of the core layer's actions on the membrane. The STL of the equivalent model is addressed through the decoupling of the forced vibration equation for a MAM carrying a petal-like core layer, subjected to sound wave excitation. The mode superposition method is employed to calculate the dynamic response of the system. The forced vibration equation is shown below:

$$T\left(\frac{\partial^2 \eta}{\partial x^2} + \frac{\partial^2 \eta}{\partial y^2}\right) - \sigma\left(\frac{\partial^2 \eta}{\partial t^2}\right) - \rho_p h(x, y, x_0, y_0, l_x, l_y)\left(\frac{\partial^2 \eta}{\partial t^2}\right) = P_{ia}e^{j\omega t} + P_{ra}e^{j(\omega t + kz)} - P_{ta}e^{j(\omega t - kz)}, \#(14)$$

where T and σ represent the tension and surface density of the membrane, respectively, while η signifies the displacement of the membrane in the out-of-plane direction. Besides, ρ_p denotes the density of the petal-like core layer, meanwhile, x, y, x_0, y_0, l_x, l_y are used to define the position and size of the equivalent additional mass. As a result of the activation of plane sound waves, leading to the transition of the system's dynamic behavior from free vibration to forced vibration, the impact of sound pressure equivalency is mathematically represented by **Eq. (14)**. Among this, P_{ia}, P_{ra}, P_{ta} are the incident, reflected and transmitted sound pressure amplitudes, respectively.

Subsequently, the forced vibration equation of the membrane is decoupled utilizing the mode superposition method, followed by the transformation of the membrane's vibration equation subject to fixed constraints through the application of the modal-type function. The out-of-plane displacement of the membrane can be expressed as[2]:

$$\eta(x, y, t) = \sum_{n=1}^{N}\sum_{m=1}^{M}\eta_{nm}(x, y)q_{nm}(t), \#(15)$$

where $\eta_{nm}(x, y)$ represents a modal-type function characterized by the membrane absent an additional

mass, while $q_{nm}(t)$ denotes the generalized coordinates associated with the modal-type function. The matrix derived in this manner conforms as:

$$- \varepsilon^2\{[M] + [Q]\}\{\tilde{q}\} + j\varepsilon[C]\{\tilde{q}\} - [K]\{\tilde{q}\} = 2P_a\{H\}, \#(16)$$

where $\{\tilde{q}\}$ represents eigenvectors, and ε denotes natural frequencies of the equivalence model. The formulas of the reflection coefficient and STL for an equivalent structure with side lengths as Lx and Ly can be written as:

$$t_p = \left| \frac{j2\rho_0c_0\varepsilon}{L_xL_y}\{H\}^T \frac{1}{-\varepsilon^2\{[M] + [Q]\} + j\varepsilon[C] + [K]}\{H\} \right|, \#(17)$$

$$STL = 20\log_{10}\frac{1}{t_p}.\#(18)$$

The STLs (below 1000 Hz) obtained by theoretical derivation and numerical simulation of the MAM carrying a petal-like core layer are shown in **Fig S4(b)**. This elucidates the advantages of utilizing petal-like metamaterials instead of conventional additional blocks, underscoring their superior performance in various applications.
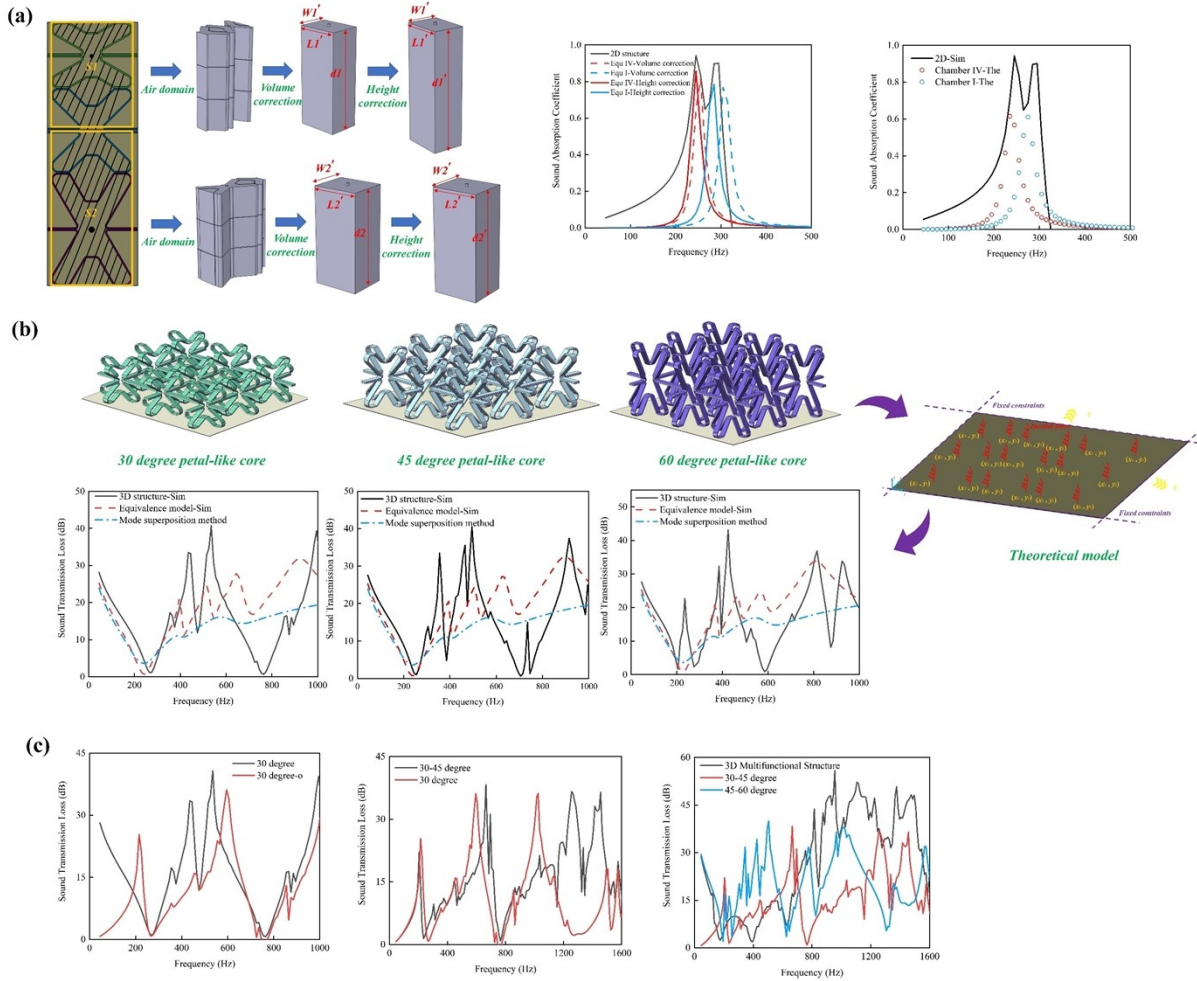

Fig. S4 Theoretical derivation of noise reduction properties of 2D/3D CFRP composite petal-like structures. (a) Equivalent models of two gradient resonant cavities. Following the volume correction, the volume of the rectangular cavity equated to that of the resonant cavity. Furthermore,

post height correction, the resonance effect of the equivalent model closely mirrored that of the original structure. A comparison is conducted between the simulation and theory outcomes of the SAC of Chamber I and Chamber IV. The theory results are obtained through the impedance matching method. (b) An equivalent method for simplifying the 3D petal-like structure. Meanwhile, the sound insulation performance of the theoretical model of the petal-like core layer with three angles is derived using the mode superposition method and compared with the numerical results. (c) A numerical model of petal-like core layers is established at different angles, demonstrating the superposition of the sound insulation effect achieved through the gradient design and rational combination of petal-like core layers, ultimately obtaining a 3D petal-like multifunctional structure with a super wideband sound insulation effect.

For the relationship between the composition of the multifunctional structure and the performance improvement, as shown in **Fig. S4(c)**, it is possible to reveal the reasons for the generation of the sound insulation bandwidth of the 3D petal-like multifunctional structure. Creating perforations in the membrane where the 30 degree and 45 degree petal-like core layers intersect can expand the local resonance band of the metamaterial by introducing an additional anti-resonance before the first-order natural frequency of the system while maintaining the existing widths of the sound isolation band. Simultaneously, the incorporation of petal-like core layers exhibiting varying mass distributions (i.e. 30 degree and 45 degree combinations) to the membrane has been observed to effectively address the sound isolation dip occurring post 1200 Hz, while also broadening the sound isolation band beyond 800 Hz. The results indicate that the gradient design led to a noticeable shift in the sound isolation band, highlighting the significant impact of the core layer on sound isolation capabilities. The broadband sound insulation performance of the final 3D petal-like multifunctional structure is attributed to the superposition effect resulting from various combinations of sound insulation features.

Part 5: Finite element method for acoustic performance analysis

A finite element model is constructed in COMSOL using the pressure acoustics and solid mechanics coupling module and its built-in narrow area acoustics. In the evaluation of sound absorption performance, an incident sound field is exclusively established on one side of the structure,

while a rigid domain is concomitantly configured on the opposing side to function as a total reflection boundary. In contrast to the aforementioned approach, the analysis of sound insulation performance involves the establishment of incident and transmitted sound fields on either side of the structure to assess the efficacy of sound wave attenuation by the structure. Boundary conditions such as supports and specified displacements around the solid material simulate the constrained form of the impedance tube. An absorbing boundary is used on the side of the air domain in the incident and transmitted sound field to simulate the infinite field without reflection.
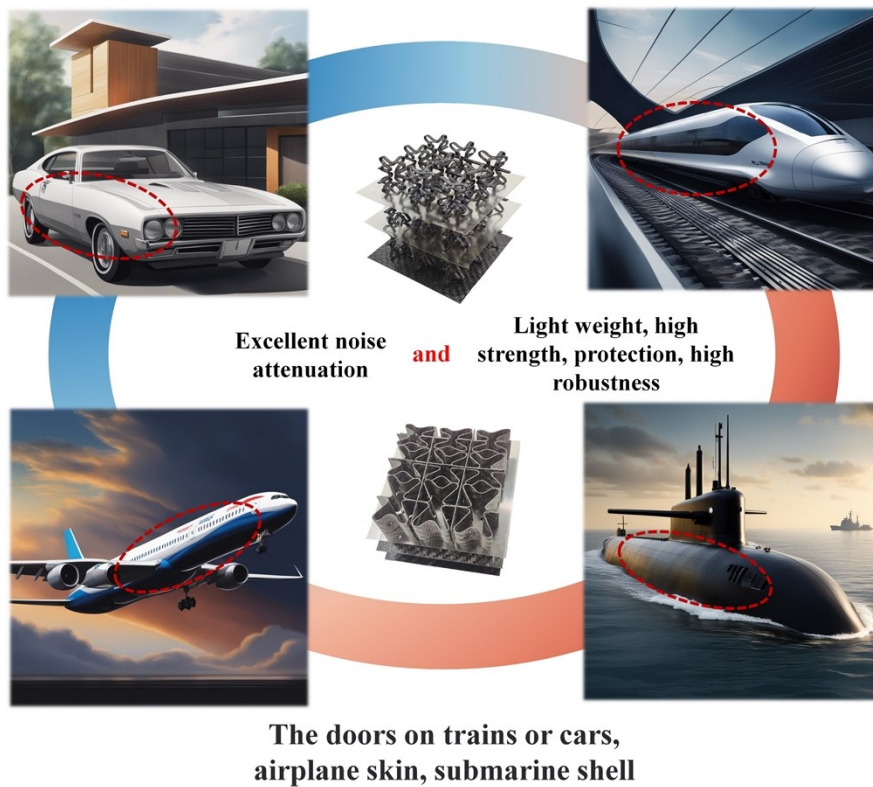
Part 6: Potential application

Fig. S5 Potential applications of 2D/3D petal-like structures in real life.

Part 7: Test method for structural deformation and failure

In order to explore the deformation ability of structure, in-plane compression of 2D composite petal-like structure was studied (**Fig. S6(a)**). Considering the impact of carbon fiber plates, membranes, and TPU shells on the compression behavior, a comprehensive examination of the structure's compression solely based on its internal components was conducted. The Poisson's ratio of petal-like structures with different angular were determined through the assessment of relative

displacements of the middle points on both sides and each individual cell in the vertical direction. The strain at the cell center was calculated by analyzing the displacement changes at specific points within the structure, namely X_{n-1}, X_{n-2}, X_{n-3}, and X_{n-4} (where n=1,2,3, and 4). Subsequently, the Poisson's ratio of the structure was derived utilizing the expression $\nu_{yx} = -\varepsilon_x/\varepsilon_y$.

Given the similarities between the 3D composite petal-like structure and the sandwich structure, as well as the negligible impact of increasing sheets on the experimental procedure, the 3D structure illustrated in **Fig. S6(a)** was utilized for monitoring cells deformations. As a result of its stacking mode, the DIC device allows for direct measurement of the displacement changes occurring at the central positions of cells on either side. This enables the direct reading of data and subsequently facilitates the incorporation of strain values into the Poisson's ratio formula for the calculation of the Poisson's ratio for each row of cells. The experimental conditions for measuring structural deformation and conducting cyclic loading experiments are illustrated in **Figs. S6(b)** and **(c)**.
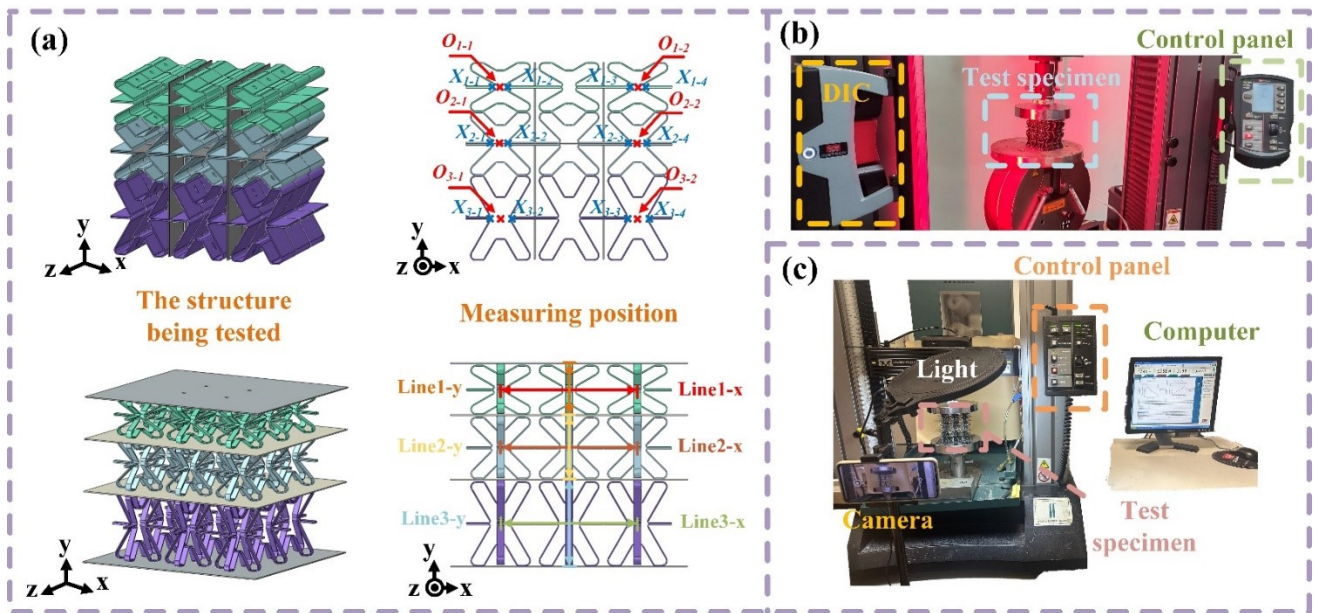

Fig. S6 Mechanical correlation experiment. (a) The 2D/3D specimens for compression experiments and the reference point positions for measuring structural deformation. (b) The deformation of the structures were measured by DIC equipment. (c) Cyclic loading and destruction experiments.

Reference

[1] Peng X, Ji J, Jing Y. Composite honeycomb metasurface panel for broadband sound absorption[J]. The Journal of the Acoustical Society of America, 2018, 144(4): EL255-EL261.

[2] Zhang Y-G, Wen J-H, Xiao Y, et al. Theoretical investigation of the sound attenuation of membrane-type acoustic metamaterials[J]. Physics Letters A, 2012, 376: 1489-1494.